Research Article

Elucidating the mechanism for high-temperature heat treatment induced embrittlement of laser-powder-based fusion manufactured NiTi alloy

Haizheng Zhang[a,b], Boyang Wu[a,b], Jiang Yi[a,b], Zhiqian Rao[a,b], Pan Wang[c], Shuai Wang[a,b,*]

[a]SUSTech Energy Institute for Carbon Neutrality, Southern University of Science and Technology, Shenzhen 518055, China

[b]Department of Mechanical and Energy Engineering, Southern University of Science and Technology, Shenzhen 518055, China

[c]Singapore Institute of Manufacturing Technology (SIMTech), Agency for Science, Technology and Research (A*STAR), 5 Cleantech Loop, 636732, Republic of Singapore

[*]Corresponding author.
E-mail address:wangs@sustech.edu.cn

ABSTRACT

Powder bed fusion-laser beam with metals (PBF-LB/M) can be used to manufacture intricate NiTi components. However, the ductility of NiTi alloys printed by PBF-LB/M is generally ~20% less than those made via conventional processes. Although many heat treatment methods have been proposed, solving this issue has been proven difficult. An intractable problem is the brittleness of PBF-LB/M-manufactured NiTi after solid solution treatment at 1000 °C. By investigating the microstructural and fractography change after heat treatment in the range of 100-1000 °C, this study found that this ductile-to-brittle transition stems from abnormal oxygen-containing Ti-rich precipitates being generated in the PBF-LB/M fabricated Ni-rich NiTi. We identified laser processing-induced local oxygen segregation and tiny TiO_2(B) particles at the fusion and grain boundaries. During the heat treatment at temperatures above 700 °C, these oxides decompose due to their low thermal stability. After this decomposition, most oxygen diffuses into the matrix, with titanium remaining in local regions. This process enriches titanium in the interfaces, forming a brittle oxygen-rich Ti_2Ni network that is known to hinder the recrystallization process in heat treatment. Furthermore, when subjected to external loading, these precipitates can induce high misfit levels and local distortion, resulting in brittle fractures along the interfaces. Based on these results, we also propose approaches to avoid high-temperature-induced embrittlement in Ni-rich NiTi.

Keywords: Laser-based powder bed fusion; NiTi; Embrittlement; Oxygen segregation; Ti_2Ni

1. Introduction

NiTi alloy is one of the most widely employed shape memory alloys [1]. Compared to Cu-based and Fe-based shape memory alloys, the austenite transformation temperature of NiTi alloys is moderate, typically occurring around room temperature [2]. Also, the shape memory effect of NiTi alloys can be fine-tuned by adjusting the alloy composition and heat treatment conditions [3,4]. This tunability renders NiTi alloys more adaptable to different engineering needs. Nevertheless, the difficult-to-machine property of NiTi alloys poses a significant obstacle for traditional manufacturing methods in addressing the demands of increasingly complex and rapid production requirements [5,6]. Hence, the additive manufacturing of NiTi alloys has attracted substantial attention [7].

Powder bed fusion-laser beam with metals (PBF-LB/M) is currently the most widely used additive manufacturing method for NiTi, offering advantages such as rapid molding speed, high precision, and the capacity to fabricate intricate structures [8,9]. However, the performance of NiTi alloys produced by PBF-LB/M has limitations. In contrast to the total elongation of >20% in traditionally manufactured counterparts [10,11], NiTi alloys manufactured by PBF-LB/M exhibit a much smaller total elongation range of 6%-15% [12,13]. Many studies posit that the properties of NiTi alloy can be further refined and enhanced through heat treatment. For instance, Saghaian et al. [14] showed a modest increase in compressive strain from ~7% to ~9% through an aging process conducted at 500 °C for 1.5 h. Carlucci et al. [15] found a 0.5%-1.0% increase in tensile strain could be achieved through a heat treatment process at 450 °C. Despite these improvements in ductility, they remain severely limited and do not approach the ductility of conventionally produced NiTi.

The underlying cause for this puzzle has been thought to be macro- and micro-defects, as well as precipitates induced by PBF-LB/M. Despite this theory, the ductility of dense samples produced via PBF-LB/M remains inferior to that of cast NiTi [13]. Therefore, we believe the most viable “smoking gun” is the presence of precipitates generated during solidification. Research by Xue et al. [16] showed that Ni-rich NiTi alloys generate oxides during the PBF-LB/M process. Although the detailed composition of the oxide was not determined, their chemical analysis indicated that these oxides are all Ti-rich. Another study by Xue et al. [17] found that the oxygen content in the PBF-LB/M process is critical to the plasticity of NiTi alloys, largely due to the effect of precipitation of Ti-rich oxides at grain boundaries during the printing process. Similar results were reported by Zhu et al. [18], who found that the printing

process of Ti-rich NiTi alloys produced Ti_2NiO_x, commonly seen in conventionally manufactured NiTi alloys. Additionally, the phase change and precipitation in Ni-rich NiTi alloys are temperature-sensitive. Typically, NiTi alloys have no precipitated phases when heat treated at 100 °C [19]. Kim et al. [20] found that the Ni_4Ti_3 phase can precipitate in Ni-rich NiTi alloys by aging at 200 °C for more than 100 h or at 300 °C for over 3 h. Zhou et al. [21] reported that Ni_4Ti_3 can also precipitate by aging at 250 °C. Frick et al. [22] found that Ni_4Ti_3 phases precipitate from NiTi alloys during heat treatment at 300-600 °C. Paryab et al. [23] found that the size of the precipitates increased during heat treatment at 600-800 °C, leading to decreased hardness. Kim et al. [24] and Khoo et al. [25] observed Ni_4Ti_3 and a small amount of Ni_3Ti in Ni-rich NiTi heat treated at 700-800 °C. Heat treatment above 800 °C is generally considered suitable for NiTi solution treatments, as it effectively removes the effects of precipitates [26–28].

To eliminate the influence of oxides, Khoo et al. [25] applied a high-temperature treatment at 700 °C to homogenize the NiTi alloy. However, the improvements in ductility and shape memory properties were insignificant, and the cause for the poor material properties remained unidentified. Chmielewska et al. [29] noted the emergence of brittle phases in PBF-LB/M fabricated NiTi after heat treatment at 900 °C and 1100 °C, but the reasons for precipitation remained unclear. These studies suggested that high-temperature heat treatment cannot improve ductility in PBF-LB/M NiTi, with the reasons for this remaining unclear. Lu et al. [30] reported that the Ti-rich phase is often a brittle phase in NiTi alloys. However, controlling the Ti-rich phase to be nano-spherical and preventing its precipitation at grain boundaries in Ti-rich NiTi alloys can improve the ductility. However, the effect of Ti-rich phases on the fracture process has not been discussed. The relationship between the precipitates generated after PBF-LB/M and high-temperature heat treatment awaits further investigation.

In this study, we systematically investigated the microstructure and properties of Ni-rich NiTi that were heat treated at temperatures ranging from 100 °C to 1000 °C. Intriguingly, we found that a 1000 °C solid solution treatment could lead to severe embrittlement of 3D-printed Ni-rich NiTi alloys. We conducted microstructural analyses to determine the cause of this embrittlement, with our results providing new insights into the precipitation behavior and failure process in PBF-LB/M fabricated Ni-rich NiTi alloys. Elucidating the embrittlement mechanism allowed us to propose approaches to mitigate the heat treatment-induced ductile-

to-brittle transition in Ni-rich NiTi alloys fabricated by PBF-LB/M.

2. Materials and methods

2.1. Materials

To compensate for the evaporation of Ni during laser printing [31], a Ni-rich NiTi powder was employed for PBF-LB/M printing. The chemical composition of raw powders was analyzed by inductively coupled plasma mass spectrometry (Agilent 7700, Agilent Scientific Instruments) (Table 1). The particle size distribution of the powder was analyzed using a laser diffraction particle size analyzer (Mastersizer 2000, Malvern Panalytical), yielding the following values: D_{10} = 20.3 μm, D_{50} = 35.0 μm, and D_{90} = 58.2 μm. To reduce oxygen content and humidity, the powder was dried in a vacuum oven at 70 °C for 12 hours before PBF-LB/M.

Table 1 Chemical composition (wt.%) of Ni-rich NiTi powder used for the PBF-LB/M process.

Ni	Fe	O	C	Ti
55.74	0.0074	0.0607	0.006	Bal.

2.2. PBF-LB/M laser parameters

The samples for testing and characterization were manufactured using a Hans-M-100 (Hans Laser, Shenzhen, China) PBF-LB/M system equipped with a continuous Yb-YAG fiber laser operating at a wavelength of 1064 nm and featuring a laser spot size of 50 μm. The scanning strategy was bi-directional with 67° rotation for each layer.

The fabrication process occurred within a chamber under argon gas at continuous flow (with purity greater than 99.999%). Our selection of parameters was initially drawn from existing studies on PBF-LB/M fabricated NiTi, particularly referencing works by Saedi et al. [32] and Yu et al. [33]. We then refined the range of manufacturing parameters on our PBF-LB/M machine, choosing parameters based on relative density and cross-sectional porosity in NiTi as the primary criteria (see Table S1 for detailed parameters in Supplementary Information). The density of the as-printed sample (three samples for each parameter) was measured by using Archimedes' method [34], and the relative density value was calculated by dividing the density of the sample by that of standard NiTi. By comparing the quality of the samples, we selected a parameter (as shown in Table 2) for printing samples in this study, as its relative density is higher than 99.99%.

Table 2 Laser parameters selected for PBF-LB/M process of NiTi in this study

Power (W)	Scanning velocity (mm/s)	Layer thickness (μm)	Hatch spacing (μm)	Energy density (J/mm^3)
200	1000	30	90	74.074

2.3. Heat treatment process

In traditionally manufactured NiTi, studies have indicated that temperatures below 300 °C are generally considered insufficient to induce changes in the microstructure [35]. The temperatures in the 300-500 °C range are known to alter NiTi alloy properties by forming precipitates such as Ni_4Ti_3 [36,37]. As the temperature increases to 500-800 °C, more precipitates are formed, and recrystallization is initiated [11,38]. The 800-1000 °C range is typically associated with the NiTi solid solution treatment [28]. Therefore, to analyze the influence of heat treatment temperature on the microstructure of PBF-LB/M fabricated NiTi, we systematically investigated the microstructure and mechanical responses for samples heat-treated at temperatures ranging from 100-1000 ℃.

The samples for heat treatment were enclosed in quartz tubes and vacuum sealed at a pressure of 1×10^{-4} Pa to avoid oxidation during heating in the furnace. The heat treatments were conducted in a box furnace (N 11/HR, Nabertherm) with a consistent 3-hour holding time, followed by water quenching. The heat-treated samples will be annotated using the heat treatment temperature and annealing duration for convenient discussion. For instance, the sample treated at 1000 ℃ for 3 h is denoted as 1000 ℃/3 h.

2.4 Density measurement

The sample size for X-ray computed tomography (CT) detection was 1.5 mm×1.5 mm×1.5 mm. The internal defects and volumetric porosity of the sample were assessed using a high-resolution Micro-CT system (D2, Diondo). The X-ray worked with a voltage of 90 kV, a tube current of 90 μA, and an integration time of 2000 ms. The voxel size for CT sampling and three-dimensional reconstruction was 0.002 mm.

2.5. Mechanical tests

To assess the mechanical properties of the samples subjected to different heat treatment processes, we fabricated dog-bone specimens for tensile testing. The dog-bone specimen utilized in this study had an overall length of 50 mm, a gauge length of 21 mm, a thickness of

2 mm, and a width of 5 mm. Tensile tests were performed using a universal testing machine at an initial strain rate of 1×10^4 s^{-1} and laboratory temperature (approximately 20 °C). To ensure the accuracy of the experimental data, an optical extensometer (Epsilon ONE, Epsilon) was employed to measure the engineering strain of the sample during loading.

2.6. Characterization methods

The sample size used for characterization was 10 mm×10 mm×5 mm. The surface morphology and defects of the samples were examined with a scanning electron microscope (SEM). For a detailed study of the crystallographic orientation and grain distribution of PBF-LB/M fabricated NiTi, we employed a high-speed electron backscatter diffraction (EBSD, Velocity, EDAX) analysis at a voltage of 20 kV and a current of 13 nA. We used the same magnification and step size (1.5 μm) to ensure accuracy. The grain size analysis was conducted using EDAX OIM Analysis software with EBSD characterization results at 120×magnification (CI>0.1, Fit<1). The average grain size of austenite across the entire sample was determined by calculating the average area of the grains and converting it to an equivalent diameter through $d=2\sqrt{A/\pi}$. To obtain clear Kikuchi diffractions in EBSD, we initially ground the sample surfaces using a mechanical polisher (LaboForce-100, Struers) and silicon carbide sandpaper with grits ranging from #180 to #2000. Subsequently, the polishing process involved the application of diamond polishing paste with particle sizes ranging from 3 μm to 0.25 μm, along with aluminum oxide polishing slurry containing 0.05 μm particles. The final step included polishing on a vibratory polisher (VibroMet 2, Buehler) with a 20 nm silicon oxide suspension.

Following the polishing process, X-ray diffraction (XRD, Smartlab, Rigaku) analysis was conducted to determine phase composition. The XRD system featured a high-flux 9 kW rotating anode X-ray source, operating at a voltage of 40 kV and a current of 150 mA, with a step size of 0.02° and a speed duration time of 15°/min.

To calculate the density and size of the precipitates, we randomly selected three areas at 1000× magnification using electron channeling contrast imaging (ECCI) in SEM and used image analysis software (ImageJ) to identify all precipitates. We calculated the average number and size (length and width) of the precipitates through particle size statistics, then divided the average number of precipitates by the area of the entire characterization region to obtain the average area density.

We used a focused ion beam (Helios 600i, FEI) with a milling area of 10 μm×10 μm to prepare electron-transparency foils for transmission electron microscopy (TEM) analysis. Microstructure features and element distribution were analyzed using a 200 kV scanning transmission electron microscope (STEM, Talos F200X, FEI) with energy-dispersive X-ray spectroscopy (EDS). High-resolution STEM images were characterized by high-angle annular dark-field (HAADF) imaging conditions using a double spherical aberration-corrected transmission electron microscope (Titan Themis G2) at 300 kV. We used simulation software (Recipro) to simulate high-resolution TEM atomic images with the following parameters: voltage 300 kV, objective aperture size 12 mrad, thickness 34 nm, and defocus -70 nm.

3. Results

3.1. Mechanical properties

We assessed the internal defects of PBF-LB/M fabricated NiTi using Micro-CT (Fig. 1(A)). The inset in Fig. 1(A) reveals that the most prominent defect does not exceed 20 μm^3, and these defects are primarily spherical, with a total volume of ~0.0011 mm^3 in a ~3.3 mm^3 region. The results confirm that the selected PBF-LB/M parameters produced a sample with volumetric porosity of about 0.003%, which matches well with the data of cross-sectional porosity obtained by SEM (Table 2). The porosity measured by Micro-CT of the as-built sample is better than that of other dense PBF-LB/M NiTi reported in studies [39]. Therefore, we consider the variation in mechanical properties to be mainly a result of the heat-treatment-induced microstructure change rather than the as-printed defects.

We applied heat treatment on the printed samples at different temperatures to observe changes in post-treatment tensile properties (Fig. 1(B)). The results reveal that the as-built sample exhibits a plateau stage between 1.5%-6% strains, with the upper plateau strength slightly increasing. In contrast, the sample treated at 300 °C shows a shorter plateau with a range of 1.5%-4.5% strains. The shorter plateau range comes at the expense of a reduction in total elongation, with a reduction percentage of 22.5%. The sample treated at 500 °C also exhibits a decrease in total elongation, but notably, the strength of the upper plateau decreases to a level below 100 MPa. The plateau in the sample treated at 700 °C was unstable, with its stress exhibiting an increasing trend after the 5% strain, indicating that the microstructure had started to change at this temperature.

After heat treatment at 1000 °C, which is generally used for solid solution treatment in traditional NiTi alloys, the apparent modulus of the sample is consistent with that of 700 °C/3 h, while the yield strength increases to 697.2 MPa. However, the stress plateau at this condition is absent, and the total elongation decreases from 9.28% to 3.83%, representing a substantial decrease of approximately 58.7%. The tensile test ends with a sharp drop at the strain-to-failure point without necking, indicating that the high-temperature heat treatment induced a typical brittle failure. To confirm whether this ductile-to-brittle transition phenomenon is unique to additively manufactured NiTi, we prepared a conventional cold-rolled NiTi plate (reduction rate 30%), performed heat treatment at 1000 °C for 3 h, and then compared the tensile properties before and after heat treatment (as shown in Fig. S1 in Supplementary Information).

It is found this ductile-to-brittle transition phenomenon does not appear in the conventional cold-rolled NiTi alloy, indicating that such phenomenon is related to the microstructural characteristics induced by additive manufacturing.

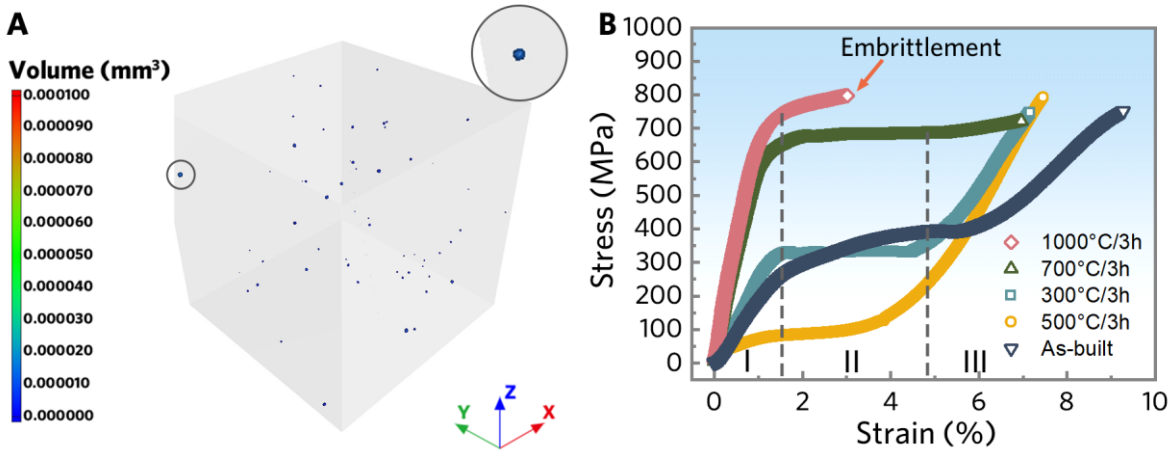

Fig. 1. (A) Three-dimensional images of defects in the as-built sample obtained using Micro-CT; the colored areas are internal defects. The inset shows a magnified view of the most prominent defect. (B) Tensile stress-strain curves of the heat-treated sample and the as-built sample.

3.2. Phase composition and surface topography

Using XRD, we characterized the phases in both as-built and samples subjected to different heat treatment temperatures (Fig. 2). The as-built sample predominantly consists of the NiTi austenite B2 phase, with a small amount of TiO_2/TiO_2(B). Because the TiO_2 and TiO_2(B) peaks are between 63.5°-64.0° in the XRD spectrum, it is difficult to distinguish them and requires further characterization in TEM. The high affinity of Ti with O leads to the inevitable production of oxides even in the Ar atmosphere in the PBF-LB/M chamber. The 300 °C heat-treated sample exhibits an emergence of Ni_4Ti_3.

Comparing the heat-treated samples at 350-500 °C (Fig. 2(B)) indicates that treatment at higher temperatures results in an increased portion of Ni_4Ti_3 and B19′ phases. In contrast, the 550-800 °C heat-treated samples exhibit an absence of Ni-rich precipitation (Fig. 2(C)), which is abnormal for the traditionally manufactured NiTi [15]. Interestingly, a small amount of Ti_2Ni phase is detected in the 800 °C heat-treated Ni-rich NiTi. Samples subjected to solution treatment at 800-1000 °C comprise only NiTi martensite and austenite (Fig. 2(D)). It is worth noting that the XRD test on the bulk sample has limited accuracy and that its results do not definitively rule out the presence of precipitates at 1000 °C. Moreover, the peaks of oxide and

Ti2Ni are weak, making it difficult to determine the phase by solely using XRD. Therefore, we will use other characterization methods, i.e., SEM, ECCI, EDS, and STEM, to confirm this abnormal phenomenon and phase later in this study.

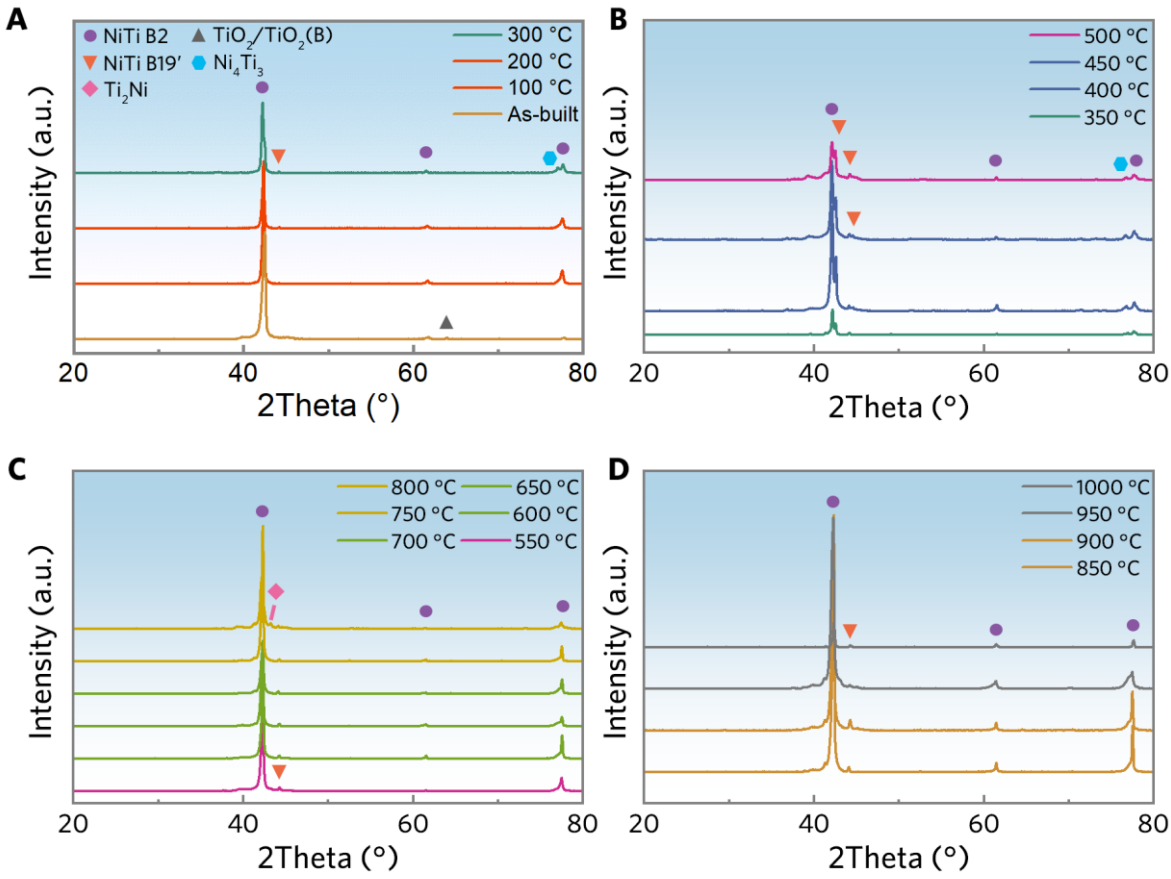

Fig. 2. XRD results of as-built and heat-treated samples at different temperatures: (A) as-built and 100 °C to 300 °C; (B) 350 °C to 500 °C; (C) 550 °C to 800 °C; (D) 850 °C to 1000 °C.

We performed a STEM characterization analysis on the as-built samples to understand the oxides present in PBF-LB/M fabricated NiTi (Fig. 3). The results suggest that the precipitates at these two locations are deficient in Ni, rich in Ti, and rich in O, with no significant change in N and C content. Similar micrographs showing such precipitates are also seen in the studies of Xue et al. [16,17]. In order to elucidate the formula of precipitates, we used the selected area diffraction pattern (SADP) in TEM to analyze their composition (Fig. 3(A) insert). By analyzing the EDS data, Fig. 3(B), we consider the precipitate as an oxide of Ti. However, by comparing the SADP with references [40,41], we found the interplanar spacing does not match the conventional rutile TiO_2. To confirm the crystal structure of these precipitates, we used HAADF imaging conditions in STEM mode to obtain their atomic contrast. As shown in Fig. 3(D) and (E), two typical shapes of precipitates, i.e., spherical particle #1 and rod-like particle

#2, are formed in the as-built NiTi, which has an austenite matrix. According to atomic image and fast Fourier transform (FFT) in the insets of Fig. 3(F) and (G), these two particles have an interplanar spacing and diffraction pattern matching well with monoclinic TiO_2(B), as reported by Feist et al. [42] and Banfield et al. [43]. The results also match well with the high-resolution TEM image simulation obtained in Recipro, as presented in the right-corner insets in Fig. 3(F) and (G). Also, we double-confirmed that the FFT diffraction pattern is located at a zone of the Kikuchi pattern of monoclinic TiO_2(B) lattice, as shown in Fig. S2. According to the HAADF analysis, the $(0\bar{1}2)$ plane normal of TiO_2(B) aligns well with the (001) plane normal of NiTi austenite. Also, there is a relationship of {010} NiTi// $\{60\bar{1}\}$ TiO_2(B). Unlike the rutile phase of TiO_2, which is very stable at high temperatures and belongs to the tetragonal crystal system, metastable TiO_2(B) belongs to the monoclinic crystal system [42,44]. In the grain interior, these tiny oxides have a size of 13.5 nm to 57.3 nm and an area density of ~44.3 μm^{-2}. At the grain boundary, the oxides have a length ranging from 18.4 nm to 71.9 nm, a width between 4.9 and 18.0 nm, and a coverage of ~13.7 μm^{-1}.

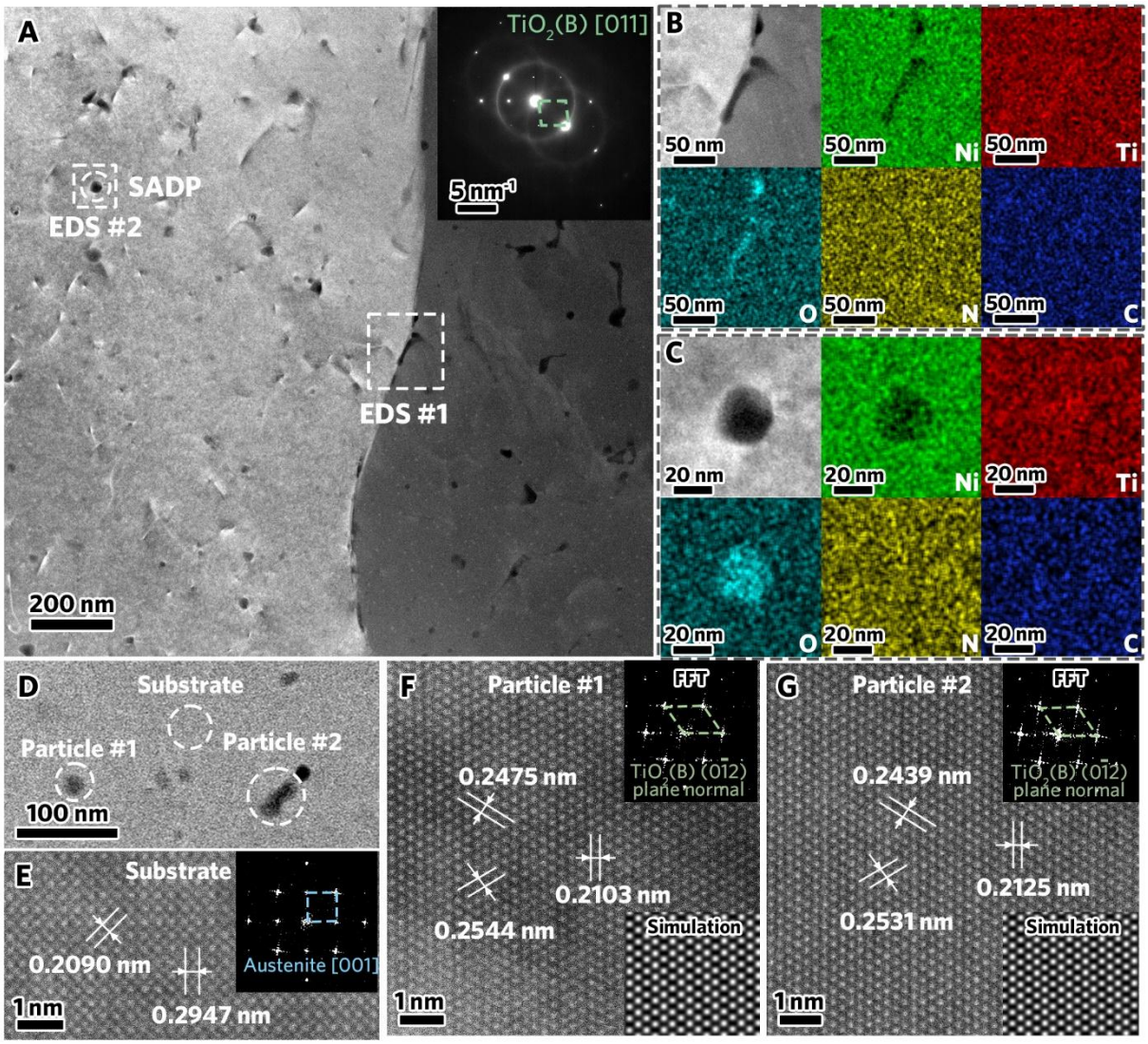

Fig. 3. STEM micrographs of precipitates in as-built sample: (A) HAADF image of grain boundaries and intragranular precipitates. The insert image shows the SADP of the circular area. The dark dots/laths indicate lower Z-contrasts, which correspond to precipitates. (B) HAADF image and EDS element distribution maps of lath-shaped precipitates at grain boundary #1 rectangular area, including Ni, Ti, O, N, and C elements. (C) HAADF image and EDS element distribution maps of dot-shaped precipitates within grain #2 rectangular area, including Ni, Ti, O, N, and C elements. (D) HAADF image of the NiTi substrate and spherical (Particle #1) and rod-shaped (Particle #2) oxides. (E) High-resolution HAADF image of the substrate, and the inset is the FFT image of the substrate. (F) High-resolution HAADF-STEM image of the spherical oxide (Particle #1), and the insets are the FFT image of the spherical oxides and high-resolution TEM simulation image. (G) High-resolution HAADF-STEM image of the rod-shaped oxide (Particle #2), and the insets are the FFT image of the rod-shaped oxide

and high-resolution TEM simulation image.

To study the evolution of precipitation after heat treatment, we observed the morphology of the cross-sectional area of both the as-built and heat-treated samples at 300 °C/3 h, 500 °C/3 h, 700 °C/3 h, and 1000 °C/3 h using ECCI in the SEM. In the as-built sample (Fig. 4(A)), the molten pool is distinctly visible with an average width of 87.7 μm, which agrees closely with the hatch spacing in PBF-LB/M. Large grains exhibit approximately rectangular shapes, located at the center of the melt pool and aligned with the laser scanning direction, with a width ranging from 67.7 μm to 85.7 μm and a length between 65.4 and 101.8 μm. The grain arrangement indicates a 67° rotation of the melt channel between layers. Multi-layered austenite grains are seen in the center of the molten pool. At the molten pool's edge, tiny equiaxed crystals appear at the intersection of two rectangular grains with a grain size of 0.2-1.5 μm.

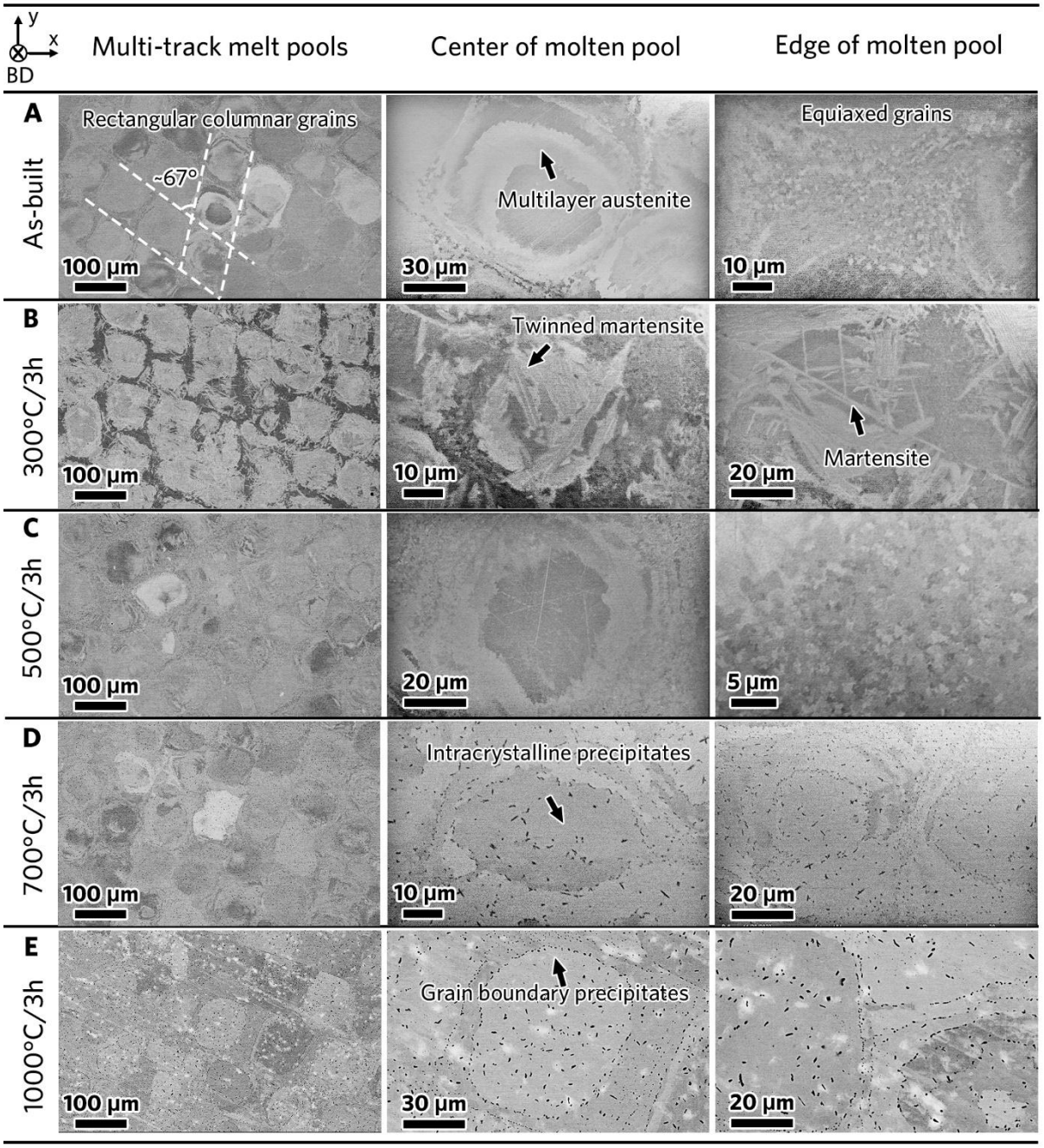

Fig. 4. Cross-sectional morphology of the as-built and heat-treated samples was examined using electron channeling contrast imaging (ECCI). Images were captured for the overall sample, center, and edge of the molten pool for each sample: (A) as-built, (B) 300 °C/3 h, (C) 500 °C/3 h, (D) 700 °C/3 h, (E) 1000 °C/3 h.

Martensite formation is seen after heat treatment at 300 °C (Fig. 4(B)). Twinned martensite is evident in the center of the molten pool, while lath martensite is present at the edge of the molten pool. The sample subjected to heat treatment at 500 °C displays a morphology similar to the as-built sample. The XRD results indicate that the 500 °C/3 h sample contains a significant amount of martensite. However, the martensite laths in this sample are not clearly

visible through ECCI. Using transmission electron microscopy, we discovered a substantial presence of nano-martensite in the 500 °C/3 h sample (as shown in Fig. S3). The nano-martensite resides within the austenite grains, which explains why it is not observed in the large-scale ECCI characterization. Based on this result, we speculate that from 300 °C to 500 °C, as the temperature increases, the form of martensite changes. The underlying reason for this transformation requires further investigation. Although nano-sized Ni_4Ti_3 is expected to be present in the grains (as shown in Fig. S3), it is not visible under the ECCI due to resolution limits [45].

Although the recrystallization temperature of the NiTi alloy is typically around 600 °C, the size and the shape of the grains in the 700 and 1000 °C heat-treated samples are still similar to those in the as-built sample (Fig. 4(C) and (D)). These results indicate recrystallization to be inhibited in the PBF-LB/M fabricated NiTi. A significant contrast of precipitates is seen in both the 700 and 1000 °C samples, following a network distribution. In the 700 °C heat-treated sample, fine precipitates are distributed along the grain boundaries, with a size ranging from 0.2 μm to 0.8 μm and a coverage of ~0.6 μm^{-1}. Inside the grains, the precipitates assume the form of long strips, with a dimension of 1 μm to 2.5 μm in length, 0.4 μm to 0.6 μm in width, and an area density of ~0.05 μm^{-2}. In the 1000 °C heat-treated sample, the precipitates are larger than those in the 700 °C treated sample, with a size of 0.6 μm to 2.5 μm at the grain boundary and a coverage of ~0.4 μm^{-1}. Inside the grains, the precipitates have a length ranging from 1.2 μm to 3.2 μm, a width between 0.9 μm and 1.3 μm, and an area density of ~0.03 μm^{-2}. The results indicate that during heat treatment at 700-1000 °C, the size of the precipitates increases while the density decreases. The crowed arrangement of precipitates along the grain boundaries can influence grain growth in the recrystallization process.

3.3. EBSD analysis results of grain orientation and precipitates

In the EBSD orientation maps, the as-built and 700 °C/3 h samples maintain a distinct molten pool shape with an interlayer angle of 67° (Fig. 5(A) and (B)), indicating that the heat treatment at 700 °C does not cause significant grain growth. However, in the 1000 °C/3 h sample, a noticeable change in grain morphology is observed. The shape of the melt pool is no longer clear (Fig. 5(C)), and the grain boundaries of the original rectangular grains are more irregular. Heat treatment at 700 °C and 1000 °C did not substantially alter the grain orientation. A statistical analysis of the average grain size of the five samples that were subjected to heat treatment at 300 °C, 500 °C, 700 °C, and 1000 °C (Fig. 5(D)) reveals that heat treatment has a

minimal effect on the average grain size (see Fig. S4 for the grain size distribution), which is different from the observed heat treatment behavior in traditional NiTi alloys [46]. The phase distribution map (CI>0.1, Fit<1) in the 1000 °C/3 h sample (Fig. 5(E)) confirms that the phases observed in Fig. 4 are Ti_2Ni. The inset in Fig. 5(E) shows that the Kikuchi patterns of Ti_2Ni and NiTi are different and both are of good quality. The average geometrically necessary density (GND) in the NiTi B2 matrix in Fig. 5(A-C) was calculated based on the method by Pantleon Field [47] (Fig. 5(F)). The comparison of GND indicated that while heat treatment can effectively reduce the dislocation density and relieve the internal stress, its effect on the distribution of the precipitates is limited.

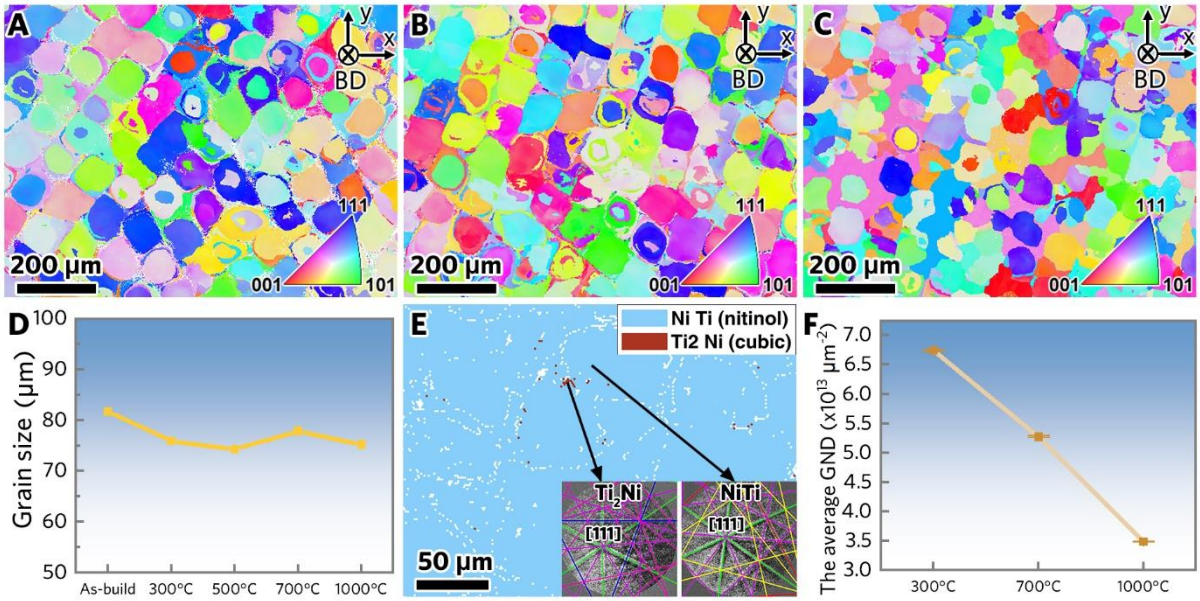

Fig. 5. EBSD analysis of both as-built and heat-treated samples: (A) IPF grain orientation map of the as-built sample. (B) IPF grain orientation map of the 700 °C/3 h sample. (C) IPF grain orientation map of the 1000 °C/3 h sample. These grains in Fig. 5(A), (B) and (C) are colored using the inverse pole figure (IPF) of crystallographic orientations that parallel the building direction (BD). (D) Comparison of the average grain size for the as-built sample and those subjected to heat treatment at 300, 500, 700, and 1000 °C, calculated based on EBSD results. (E) EBSD phase distribution map of the 1000 °C/3 h sample (CI>0.1, Fit<1), the insets show the Kikuchi patterns of Ti_2Ni and NiTi. (F) Comparison of GND for the as-built samples and heat-treated samples, calculated based on EBSD results (CI>0.1, Fit<1).

3.4. Precipitate analysis in 1000 °C/3 h sample

A detailed analysis of the elemental composition of the precipitates in the 1000 °C/3 h sample

(Fig. 6) reveals that the precipitates are found at both the grain boundaries and within the grains of the 1000 °C/3 h sample (Fig. 6(A)). Fig. 6(B-E) reveals the precipitates at the grain boundaries and within the grains to be deficient in Ni, abundant in Ti, and enriched in O and N. The EDS mapping in SEM confirms that the precipitates at the grain boundaries and within the grains are similar.

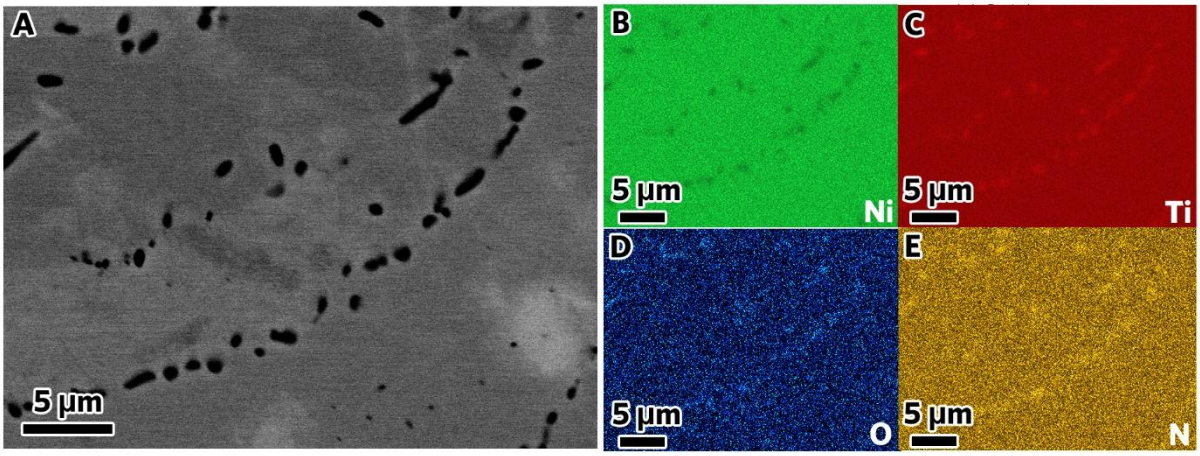

Fig. 6. EDS analysis of precipitates in 1000 °C/3 h sample by SEM. (A) Morphology of precipitates at grain boundaries and within grains, and corresponding elemental distribution mappings of (B) Ni, (C) Ti, (D) O, and (E) N.

We further conducted STEM micro-scale analysis on the 1000 °C/3 h sample, with diffraction analysis confirming that this precipitate is Ti_2Ni (Fig. 7(A) and (B)) and the EDS maps of Ni, Ti, O, N, and C in STEM (Fig. 7(C-G) respectively) agreeing well with the SEM observation. All these results confirm that the main composition of the precipitate is Ti_2Ni, with a small amount of O and N in solution. Ti_2Ni has a certain solubility for oxygen, and the presence of interstitial oxygen atoms helps to stabilize Ti_2Ni [48]. Some studies have referred to this Ti_2Ni phase in the presence of interstitial oxygen atoms as $Ti_4Ni_2O_x$. However, Frenzel et al. [3] have pointed out the lack of crystallographic evidence for this designation. Therefore, it is referred to as oxygen-rich Ti_2Ni in this study. Local distortion is induced by the precipitation behavior (Fig. 7(H)). We used an SADP analysis to analyze the misfit of the matrix and precipitate (Fig. 7(I, J)). The resulting SADP matrix belongs to the [100] zone axis of NiTi austenite, with a lattice constant of 2.79 Å. Comparing the orientation of the precipitates and the matrix reveals an evident incoherent relationship between the matrix and precipitate. Studies have confirmed the existence of a semi-coherent and incoherent relationship between NiTi-B2 phase and oxygen-rich Ti_2Ni. At the same time, the growth of precipitates with increasing temperature, transitioning from a semi-coherent to an incoherent state has also been reported [49,50]. This

incoherent relationship induces a local strain field in the matrix around the precipitate, which can serve as a cracking initiation site. This strain field arises from the incoherent relationship between Ti_2Ni and the NiTi matrix [51]. Additionally, the precipitation of Ti_2Ni in NiTi alloys typically modifies the Ni/Ti atomic ratio along the precipitate-matrix interface [52], which can induce local lattice distortion and cause heterogeneous responses under external loading.

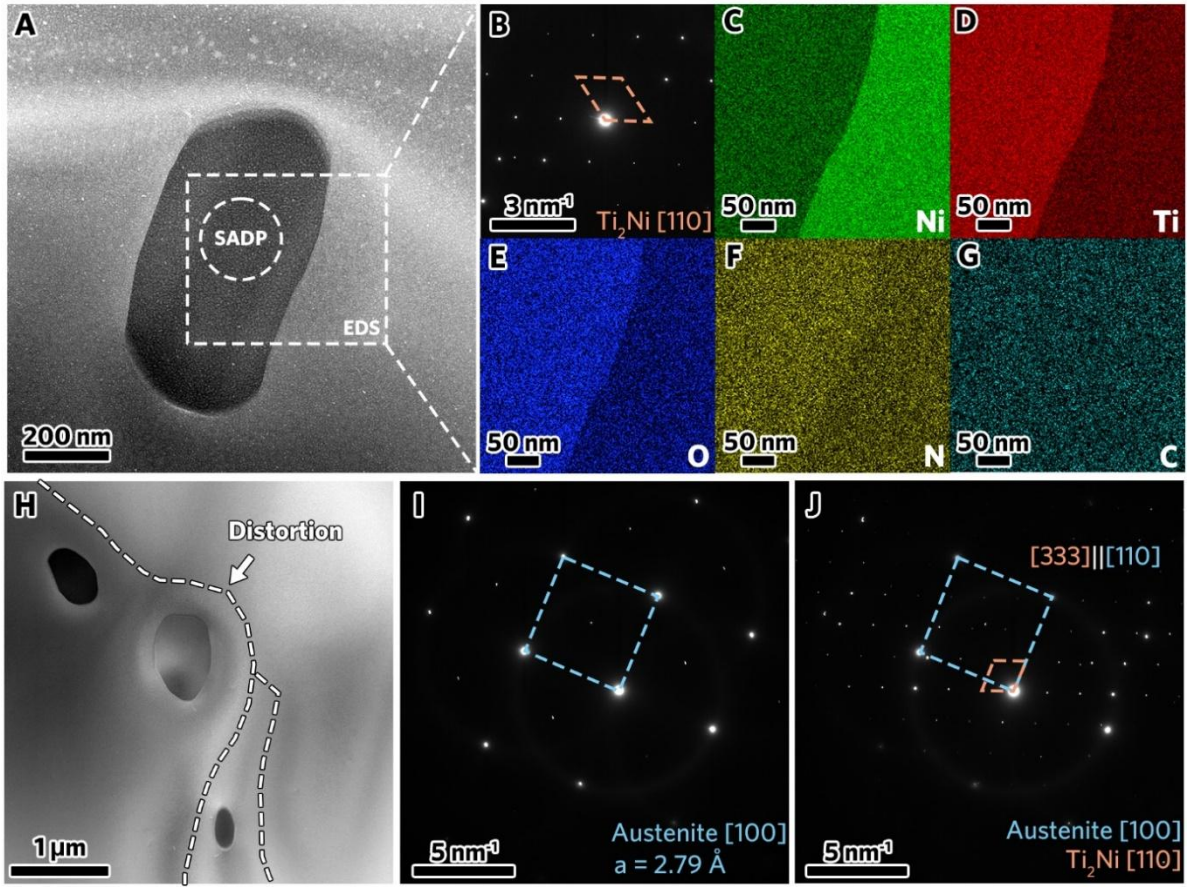

Fig. 7. STEM micrographs and diffractions of precipitates in 1000 °C/3 h sample: (A) HAADF image of individual precipitates. (B) SADP of the circular area from Fig. 7(A) and corresponding elemental distribution mappings of (C) Ni, (D) Ti, (E) O, (F) N, and (G) C. (H) STEM image of three precipitates and the matrix, including matrix lattice distortion. (I) SADP of NiTi matrix. (J) SADP of NiTi matrix and precipitates.

3.5. Fracture morphology of as-built and heat-treated samples

Examining the fracture morphology of the as-built sample (Fig. 8), reveals discernible cleavage steps and dimples on the fracture surface, accompanied by cracks extending along the grain boundaries (Fig. 8(A)). Magnifying this reveals a large cleavage facet resulting from cracking along the grain boundaries decorated by several oxides (Fig. 8(B)). Despite the overall

prevalence of cleavage characteristics in the as-built sample, many dimples are dispersed along the cleavage steps (Fig. 8(C)). This observation suggests that although a ductile fracture mode predominates in the as-built sample, oxides along grain boundary can induce brittle features in the local region.

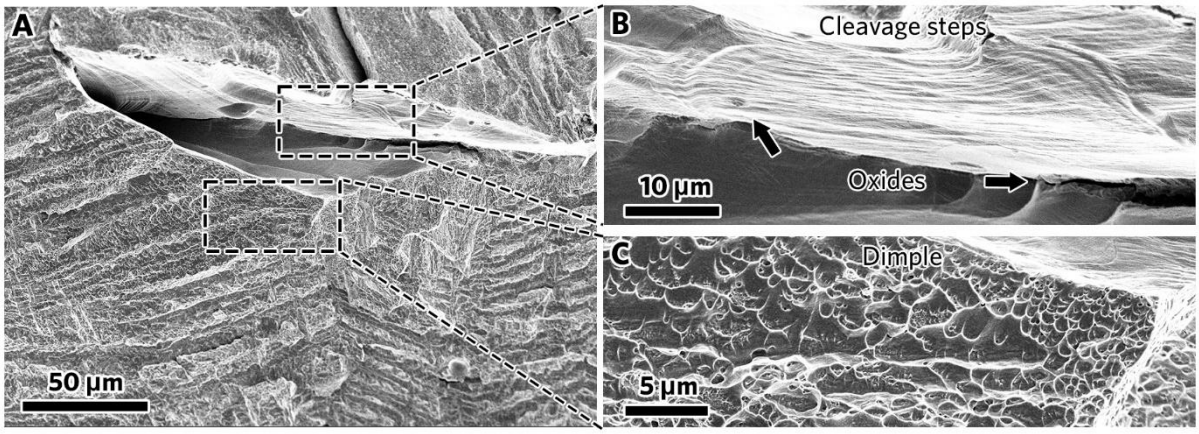

Fig. 8. Fracture morphology of the as-built sample: (A) an overview, (B) cleavage steps and oxides along the grain boundaries that can be observed by enlarging the crack in Fig. 8(A), (C) dimples that can be observed by enlarging the surface in Fig. 8(A).

In the fracture morphologies of the 500 °C/3 h and 1000 °C/3 h heat-treated samples (Fig. 9), there is a notable absence of dimples in the 500 °C/3 h sample compared to the as-built sample (Fig. 9(A)). Instead, a substantial number of cleavage steps is prominent. Magnifying these reveals cracking characteristics along the edge of the molten pool (Fig. 9(B)). The fracture morphology of the 1000 °C/3 h sample (Fig. 9(C)) reveals fewer small facets appearing on the cleavage feature, and many cracks propagating along the grain boundaries. Analyzing the precipitates along the cleavage plane here using the backscatter detector in SEM (Fig. 9(D)). highlights regions with lower average atomic numbers with darker contrast. The EDS results of the precipitates on the fracture surface (Fig. 9(E)) are consistent with the presence of Ti_2Ni (Fig. 6). The fractography analysis indicates that the oxygen-rich Ti_2Ni precipitates can assist in the fracture process of high-temperature heat-treated samples.

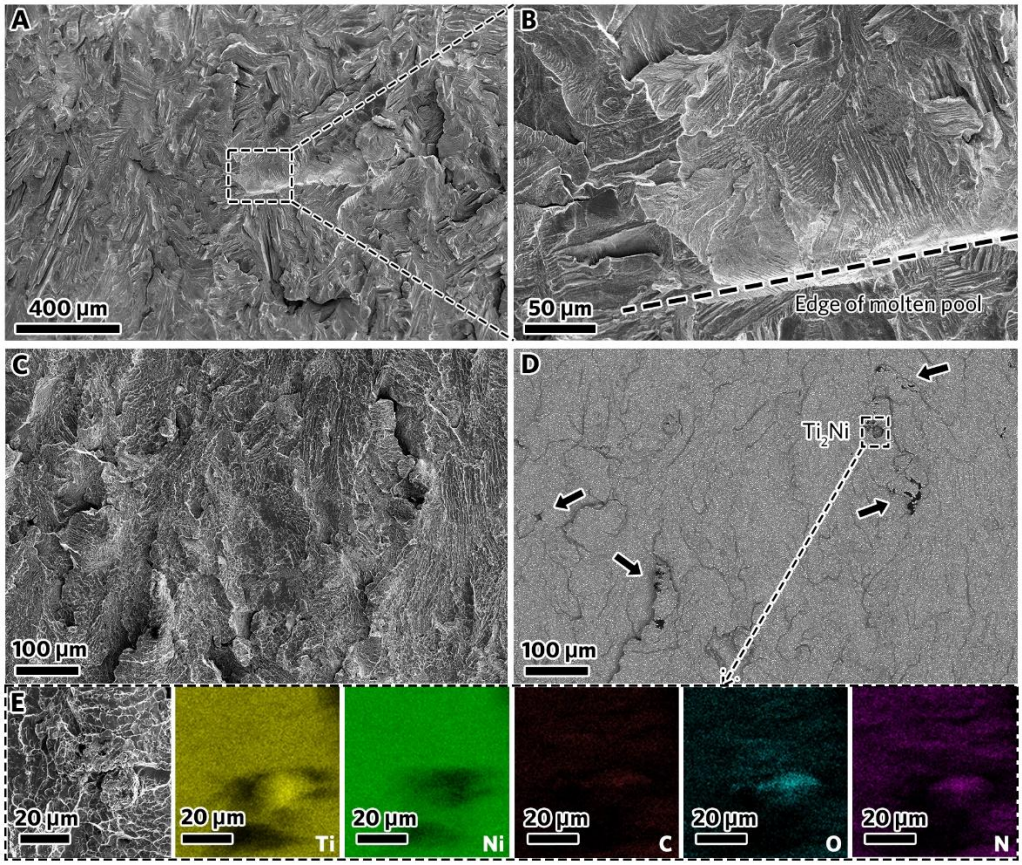

Fig. 9. Fracture morphology of the 500 °C/3 h and 1000 °C/3 h sample: (A) an overview of the 500 °C/3 h sample, (B) fracture characteristics along the melt pool observed by enlarging Fig. 9(A), (C) an overview of the 1000 °C/3 h sample, (D) image observed by using backscattered electrons detectors in the area of Fig. 9(C), (E) EDS results of precipitate on the fracture surface in Fig. 9(D).

4. Discussion

4.1 Effect of precipitates on the matrix lattice constant

In the selected area diffraction pattern (SADP) of the as-built, 500 °C/3 h, and 1000 °C/3 h samples (Fig. 10), the lattice constants of the NiTi matrix in the three samples can be determined by calculating the interplanar spacing of the NiTi austenite (110) crystal plane. Compared with the as-built sample, the lattice constant of the matrix at 500 °C/3 h increases by 4.4%, while the lattice constant of the matrix at 1000 °C/3 h decreases by 5.1%. Due to the atomic radii of Ni and Ti differing by 1.47 Å [53], the lattice constants of Ni-rich and Ti-rich NiTi alloys differ. Therefore, the change in the lattice constant of NiTi austenite is directly associated with the Ni/Ti atomic ratio. A Ni/Ti atomic ratio of 1 corresponds to a lattice constant of ~3.00 Å for NiTi austenite [54]. Ni-rich NiTi alloys typically have a lattice constant smaller than 3.00 Å, whereas Ti-rich NiTi alloys usually have a lattice constant greater than 3.00 Å. Because the matrix lattice constant of the as-built sample is less than 3.00 Å, it should have an initial Ni-rich state.

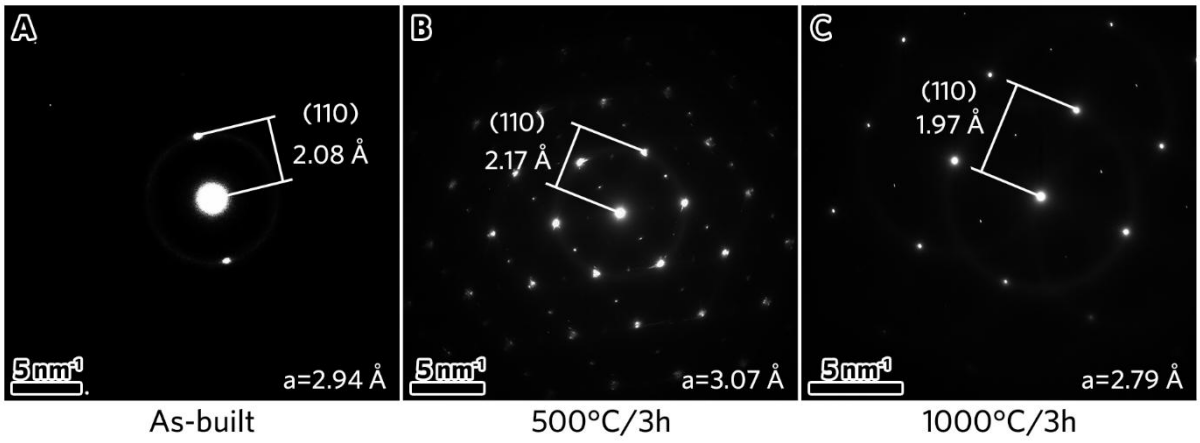

Fig. 10. SADP of as-built, 500 °C/3 h, and 1000 °C/3 h samples, the interplanar spacing of NiTi austenite (110) crystal plane, and the lattice constant of NiTi austenite were calculated: (A) as-built, (B) 500 °C/3 h, (C) 1000 °C/3 h.

In the 500 °C/3 h sample, the increase in the matrix lattice constant is attributed to the Ni-rich precipitate Ni_4Ti_3, which appears between 300-500 °C; this has been confirmed by our XRD analysis. Our previous study [45] and that by Liu et al. [55] both found the precipitation of Ni_4Ti_3 in a Ni-rich NiTi alloy by subjecting it to aging at 300 °C for 2 h. Khalil-Allafi et al. [37] and Michutta et al. [56] also found precipitation of Ni_4Ti_3 through aging at a higher temperature of 500 °C.

By contrast, the decrease in the matrix lattice constant in the 1000 °C/3 h sample is closely linked to the increase in the matrix Ni/Ti element ratio caused by Ti-rich precipitate Ti_2Ni. However, Ti-rich phases in Ni-rich NiTi alloys have not been reported as far as we know. In Ti-rich NiTi alloys, studies by Lu et al. [30], Ahadi and Rezaei [57], Bhagyaraj et al. [52], and Chen et al. [50] have reported precipitation of Ti_2Ni via heat treatment in the temperature range of 500-750 °C. Understanding the formation mechanism and the evolution process of Ti_2Ni in the PBF-LB/M fabricated Ni-rich NiTi is essential for further discussions on its mechanical behavior.

4.2 Precipitation behavior of printed samples during high-temperature heat treatment

A Ti-rich phase does not normally occur in Ni-rich NiTi alloys. The precipitation of Ti-rich phases in NiTi alloy is usually associated with elements with a high affinity to Ti. Tadayyon et al. [58] observed mixed precipitation of Ti_2Ni and TiO_2 during the solid solution treatment of a Ti-rich NiTi alloy at 900 °C/2 h. Rehman and Nam [59] introduced a trace amount of elemental N to a NiTi alloy and found the precipitation of Ti_2Ni. Ti_2Ni is thermodynamically unstable at high temperatures. However, it has been widely accepted that oxygen can act as an interstitial stabilizer to Ti_2Ni at high temperatures [48], and oxygen-rich Ti_2Ni is more stable in a Ni-rich system [60]. Therefore, we postulate that the observed enrichment of O and N elements in Ti_2Ni in the 1000 °C/3 h sample is linked to the precipitation behavior.

In the as-built samples, we observed TiO_2(B) phases, which are sub-stable phases, unlike the high-temperature stabilized TiO_2 rutile phase [42]. Yoshida et al. [61] pointed out that TiO_2(B) can be prepared under certain high temperature and pressure conditions. During the PBF-LB/M process, the NiTi melt pool undergoes rapid cooling and heating, and Ni evaporation may temporarily form a pressure cavity locally, where elements such as O and N exist, and the instantaneous temperature reaches 3000 °C [62,63]. Therefore, we speculate that the evaporated Ni vapor and the high-temperature environment in the melt pool during the PBF-LB/M process may have led to the local production of TiO_2(B). Sabbagh et al. [64] and Wang et al. [65] have shown the difficulty in maintaining the crystal structure of TiO_2(B) above 700 °C, and suggested that TiO_2(B) may decompose in the NiTi matrix upon heating to 700 °C. This decomposition results in Ti and O enrichment in the local region and encourages the formation of new phases.

Among all Ni-Ti binary compounds, Ti_2Ni possesses a low formation enthalpy (-0.278 eV/atom), indicating a more stable crystal structure than the others [66–70]. The reaction Gibbs free energy of Ti_2Ni at high temperatures is negative (-71428.7 J/mol at 900 °C) and much lower than that of NiTi (-61416.5 J/mol at 900 °C) [71,72]. These can act as a driving force to form Ti_2Ni when heat-treated at high temperatures. Our observation of Ti_2Ni particles around the fusion boundary corroborates the findings of high-temperature laser cladding studies by Lv et al. [73] and Song et al. [74]. The diffusion rate of O in NiTi is also much higher than that of Ti [75], leading to most of the decomposed oxygen diffusing to other trapping sites during the heat treatment process. There should also be some residual oxygen that dissolves in Ti_2Ni. This explains the coexistence of oxide and Ti_2Ni at the same intercrystalline and grain boundary locations in both the as-built and 1000 °C/3 h samples.

According to the results and discussion, we have drawn schematic diagrams for the precipitation behavior during high-temperature heat treatment and presented them in Fig. 11. In Fig. 11(A), the PBF-LB/M process shows an interlayer rotation angle of 67°, leading to the formation of rectangular grains in Fig. 11(B). On the edge of the molten pool of as-built NiTi alloy (Fig. 11(C)), the oxygen segregation and TiO_2(B) are locally distributed along the grain boundaries, within the grains, and also along the boundary between regions of fine equiaxed grains and rectangular grains. The fine equiaxed crystals at the edge of the molten pool are influenced by the temperature gradient within the pool. Simulation results from Ninpetch et al. [76] indicate that while the scanning velocity has little effect on the temperature at the center of the molten pool, it significantly impacts the temperature gradient from the center to the edge. When the scanning velocity increases from 400 mm/s to 800 mm/s, the temperature difference from the center to the edge of the molten pool rises from approximately 525 °C to approximately 1050 °C. In this study, a scanning velocity of 1000 mm/s was used, resulting in a significant temperature gradient from the center to the edge. There are many nucleation points at the edge of the molten pool due to the contact with the substrate and the flow of the molten pool during the manufacturing process. The increase in the temperature gradient from the edge to the center of the molten pool leads to greater supercooling. Together, these factors cause the nucleation rate to increase faster than the growth rate of the crystal nuclei, resulting in many equiaxial grains. Generally, when the scanning strategy in PBF-LB/M is uni-directional or zigzag (0° or 180° rotating), the remelting in the laser deposition process should strongly affect the edge of previously molten pools, even if these melts have a convex shape and induce coarsening of equiaxed grain. However, the scanning strategy used in this study is 67° rotating,

and the laser energy is concentrated in only tens of micros, these two factors together inhibited the remelting of the convex melt edge. This results in the retention of numerous molten pool edges, which contribute to forming many equiaxed grains throughout the sample, as shown in the results in Fig. 4(A). Oxygen may arise from the production of NiTi powders and the environment in the PBF-LB/M chamber, and it is very difficult to limit due to the high affinity of Ti and oxygen.

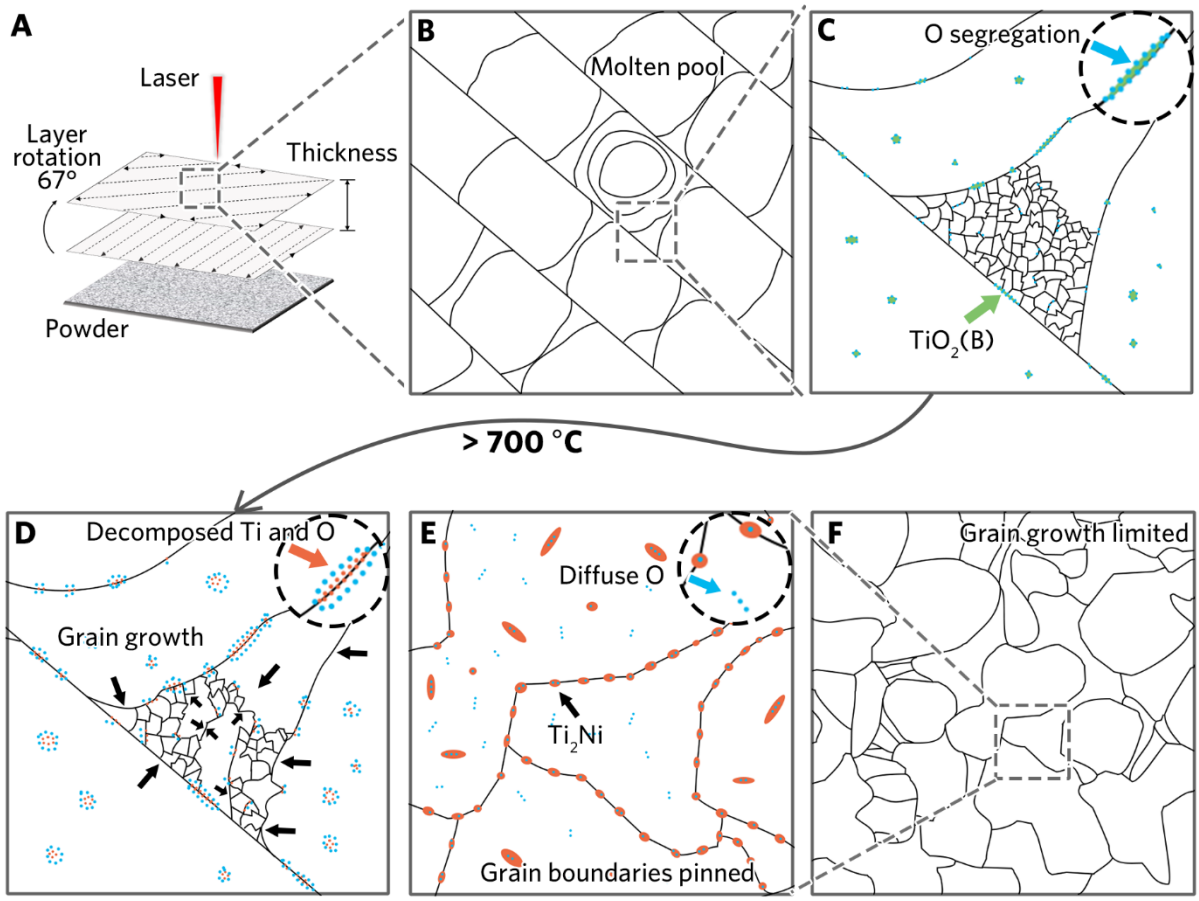

Fig. 11. Schematic representation of the precipitation behavior in PBF-LB/M NiTi alloy: (A) Overview of the PBF-LB/M process. (B) Representation of the multi-track melt pool and grain morphology of NiTi alloy in the printed state. (C) Detailed schematic of grain boundaries and the fine grain zone at the edge of the molten pool of NiTi alloy in the printed state, shown in magnification. (D) Illustration of the precipitation and recrystallization process of PBF-LB/M fabricated NiTi during heat treatment above 700 °C. (E) Schematic depiction of grain boundaries and precipitates in PBF-LB/M fabricated NiTi alloy after heat treatment. (F) Representation of the polycrystalline grain morphology of PBF-LB/M fabricated NiTi alloy after heat treatment.

At a treatment temperature beyond 700 °C, TiO_2(B) undergoes decomposition, causing part of O to diffuse into the NiTi matrix (Fig. 11(D)). Subsequently, Ti_2Ni starts forming in the locations initially occupied by the oxide. The remaining O is dissolved in Ti_2Ni and plays a stabilizing role. Simultaneously, austenite grain boundaries commence migration during the recrystallization process, eliminating fine grains. However, because of the incoherent misfit between oxygen-rich Ti_2Ni at the grain boundaries and the matrix, which produces a pinning effect of oxygen-rich Ti_2Ni on the grain boundaries, the migration of long grain boundaries is hindered. The relationship between the precipitates and the grain boundaries (Fig. 11(E)) allows one to observe irregular grain boundaries having a uniform distribution of oxygen-rich Ti_2Ni in the 1000 °C/3 h sample (Fig. 11(F)).

4.3 Effect of heat treatment on mechanical properties

The formation of high-density Ti-rich precipitates is expected to strongly influence the mechanical response of NiTi alloy. Liu et al. [78] categorized the tensile mechanical behavior of NiTi into four stages (I, II, III, IV), each with distinct deformation mechanisms closely related to microstructure. The Young's moduli of the as-built, 300 °C/3 h, and 500 °C/3 h samples fall within the range of martensite values for conventionally manufactured NiTi (Fig. 12(A)), indicating the involvement of martensitic transformation in Stage I of these samples. The dislocation structure and precipitates in the as-printed sample would be the main contributors that accelerate the stress-induced martensitic phase transformation process. After 300 °C/3 h and 500 °C/3 h heat treatment, martensite was formed according to our XRD and EBSD observation, and as a result, the modulus can decrease to values lower than that of the as-printed one. In contrast, Young's modulus of the 700 °C/3 h and 1000 °C/3 h samples are much higher (at a level of conventionally manufactured NiTi austenite). This change can be attributed to the formation of high-density Ti-rich precipitates. The precipitation behavior can increase the Ni/Ti atomic ratio in the matrix and correspondingly increase the modulus to a value close to that for a Ni-rich NiTi alloy [79], in which the austenite phases are stabilized for the high Ni concentration.

In comparing the upper plateau stress in Stage II for all samples (Fig. 12(B)), the 300 °C/3 h sample was found to have a slightly lower upper plateau stress than the as-built sample. This is attributed to the elimination of dislocations and precipitation of Ni_4Ti_3. In the 500 °C/3 h sample, the influence of such change in microstructure becomes stronger and manifests as a significant decrease in upper plateau stress. The upper plateau stress of the 700 °C/3 h sample

increases due to the precipitation of oxygen-rich Ti_2Ni.

The 1000 °C/3 h sample shows no stress-induced phase transformation (Fig. 1(B)), making it unfeasible to classify the 1000 °C/3 h sample following the deformation response rule of the NiTi alloy (strictly speaking, there is no Stage II or III here). Therefore, its upper plateau stress is defined using its ultimate stress (Fig. 12(B)). Our results suggest that high oxygen-rich Ti_2Ni precipitation raises the stress required for the martensitic phase transformation to a higher level than its ultimate stress.

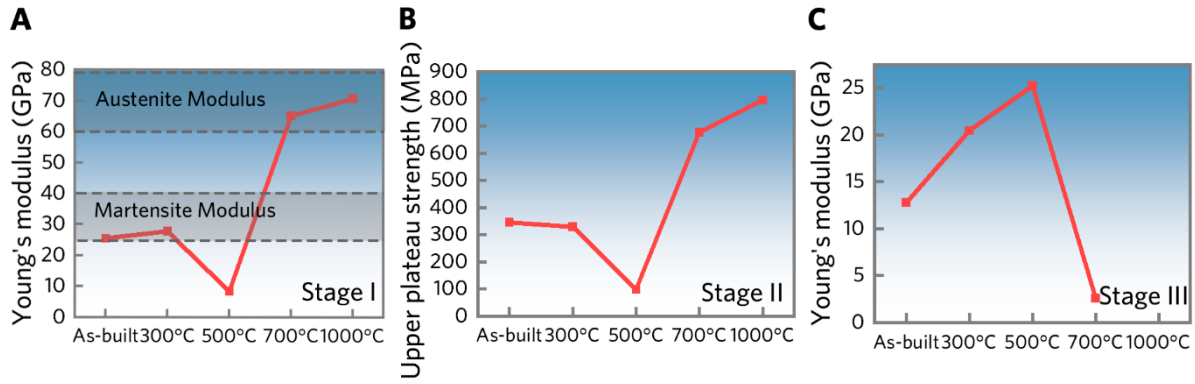

Fig. 12. Comparison of mechanical responses of as-built and heat-treated samples: (A) Young's modulus in stage I. For convenient discussion, the ranges of austenite and martensite modulus for NiTi are annotated by dashed lines in Fig. 12(A), which are collected from the literature [77]. (B) Upper plateau strength in stage II. (C) Young's modulus in stage III.

Stage III of tensile deformation involves a complex interplay of martensitic phase transformation, martensitic elastic deformation, and plastic deformation. A comparison of Young's modulus in Stage III (Fig. 12(C)) shows that the contribution of martensitic elastic deformation is the highest at 500 °C/3 h, followed by 300 °C/3 h, then as-built, and lowest at 700 °C/3 h. This difference is likely also related to precipitation behavior. The Ni_4Ti_3 precipitation in low-temperature heat-treated samples lowers the stresses required for martensitic phase transformation, making it occur more readily in Stage II and with the greatest contribution of martensitic elastic deformation in Stage III. By contrast, samples with more oxygen-rich Ti_2Ni precipitation need higher stresses for martensitic phase transformation, making martensitic transformation more difficult. Thus, Stage III of 700 °C has the least contribution of martensitic elastic deformation and the lowest modulus. The brittlement capability of the oxygen-rich Ti_2Ni precipitates and the lattice distortion around them, resulting

from the incoherent relationship between oxygen-rich Ti_2Ni and the matrix, are key factors that contribute to the brittle fracture of the 1000 °C/3 h sample. However, Lu et al. [30] suggested that the homogeneous nano-spherical Ti_2Ni phase could enhance the elongation of Ti-rich NiTi alloys. This is different from the non-spherical, coarse Ti_2Ni distributed along grain boundaries found in this study. How to modulate the distribution, shape, and size of the Ti_2Ni phase in Ni-rich NiTi alloys remains to be investigated.

Based on the above, inhibiting the generation of oxides during the PBF-LB/M process is considered the primary approach to producing additively manufactured NiTi with a ductility similar to its conventionally produced counterpart. Effective methods for attaining this goal include using oxygen-free NiTi powders and introducing a small amount of hydrogen to prevent oxidation during PBF-LB/M. The success of these strategies will be extensively evaluated in future studies.

5. Conclusions

In summary, the important findings of this study are summarized as follows:

(1) After high-temperature solid solution heat treatment, we observed abnormal precipitation of oxygen-containing Ti-rich particles (Ti_2Ni) in PBF-LB/M fabricated Ni-rich NiTi alloy. This abnormal Ti-rich precipitate can inhibit recrystallization during heat treatment and induce brittle failure in the presence of external loading.

(2) The formation of oxygen-rich Ti_2Ni precipitates is attributed to the decomposition of PBF-LB/M-induced TiO_2(B). The TiO_2(B) is unstable at temperatures higher than 700 °C, and its decomposition induces high Ti-concentration regions near fusion lines and grain boundaries, which prompts the formation of an oxygen-rich Ti_2Ni network.

(3) Our study indicates that owing to the incoherent relationship between the Ti-rich precipitate and matrix, these precipitates impose a pinning effect on grain boundary growth during high-temperature heat treatment, consequently limiting the recrystallization process. Furthermore, Ti-rich precipitates at the grain boundaries can cause brittle fractures when subjected to a tensile test at room temperature.

Acknowledgements

This work is financially supported by the National Key R&D Program of China (No. 2022YFB4600700). The authors gratefully acknowledge the support from the Shenzhen Science and Technology Innovation Commission through awards (Nos. JCYJ20210324104414040, 20220530114400001 and 20220815150609002). SW acknowledges support from the Key-Area Research Project of the Guangdong Province Department of Education (No. 2022ZDZX3021) and the High Level of Special Funds (No. G03034K001). The authors gratefully acknowledge the support from the Guangdong Basic and Applied Basic Research Foundation through awards (No. 2024A1515010358). All authors gratefully acknowledge the assistance from Dr. Yang Qiu and Dr. Dongsheng He at SUStech Core Research Facilities. We thank the electron microscope center of KAIPLE Co. Ltd (Changsha) for the support of microstructural characterizations.

Data availability

The raw/processed data required to reproduce these findings cannot be shared at this time as the data also forms part of an ongoing study.

Declaration of competing interest

The authors declare that they have no known competing financial interests or personal relationships that could have appeared to influence the work reported in this paper.

Credit authorship contribution statement

Haizheng Zhang: Conceptualization, Methodology, Investigation, Writing - original draft.
Boyang Wu: Investigation, Writing - original draft.
Jiang Yi: Investigation, Writing - original draft.
Zhiqian Rao: Investigation, Writing - original draft.
Pan Wang: Investigation, Writing - review & editing.
Shuai Wang: Writing - review & editing, Supervision, Funding acquisition, Conceptualization.

References

[1] W. Huang, Mater. Des. 23 (2002) 11-19.
[2] C. Velmurugan, V. Senthilkumar, S. Dinesh, D. Arulkirubakaran, Mater. Today Proc. 5 (2018) 14597-14606.
[3] J. Frenzel, E.P. George, A. Dlouhy, C. Somsen, M.F.-X. Wagner, G. Eggeler, Acta Mater. 58 (2010) 3444-3458.
[4] S. Saedi, A.S. Turabi, M. Taheri Andani, C. Haberland, H. Karaca, M. Elahinia, J. Alloy. Compd. 677 (2016) 204-210.
[5] K. Weinert, V. Petzoldt, Mater. Sci. Eng. A 378 (2004) 180-184.
[6] H. Wang, B. Wang, Z. Liu, Z. Li, H. Liu, Q. Song, Mater. Des. 236 (2023) 112496.
[7] Y. Feng, B. Liu, X. Wan, Q. Liu, X. Lin, P. Wang, J. Alloy. Compd. 908 (2022) 164568.
[8] X. Li, P. Wang, M. Zhao, X. Su, YH. Tan, J. Ding. Addit Manuf. 89 (2024) 104248.
[9] B. Zhang, P. Wang, Y. Chew, Y. Wen, M. Zhang, P. Wang, G. Bi, J. Wei, 794 (2020) 139941.
[10] W. Elkhal Letaief, T. Hassine, F. Gamaoun, Mater. Sci. Technol. 33 (2017) 1533-1538.
[11] H. Sadiq, M.B. Wong, R. Al-Mahaidi, X.L. Zhao, Smart Mater. Struct. 19 (2010) 035021.
[12] Z. Xiong, Z. Li, Z. Sun, S. Hao, Y. Yang, M. Li, C. Song, P. Qiu, L. Cui, J. Mater. Sci. Technol. 35 (2019) 2238-2242.
[13] S. Wei, J. Zhang, L. Zhang, Y. Zhang, B. Song, X. Wang, J. Fan, Q. Liu, Y. Shi, Int. J. Extreme Manuf. 5 (2023) 032001.
[14] S.E. Saghaian, M. Nematollahi, G.P. Toker, N.S. Moghaddam, S.M. Saghaian, M. Radhakrishnan, O. Anderoglu, M. Elahinia, H. Karaca, Shape Mem. Superelast. 9 (2023) 192-206.
[15] G. Carlucci, L. Patriarca, A.G. Demir, J.N. Lemke, A. Coda, B. Previtali, R. Casati, Shape Mem. Superelast. 8 (2022) 235-247.
[16] L. Xue, K.C. Atli, S. Picak, C. Zhang, B. Zhang, A. Elwany, R. Arroyave, I. Karaman, Acta Mater. 215 (2021) 117017.
[17] L. Xue, K.C. Atli, C. Zhang, N. Hite, A. Srivastava, A.C. Leff, A.A. Wilson, D.J. Sharar, A. Elwany, R. Arroyave, I. Karaman, Acta Mater. 229 (2022) 117781.
[18] J.-N. Zhu, W. Zhu, E. Borisov, X. Yao, T. Riemslag, C. Goulas, A. Popovich, Z. Yan, F.D. Tichelaar, D.P. Mainali, M. Hermans, V. Popovich, J. Alloy. Compd. 967 (2023) 171740.
[19] A.R. Pelton, T.W. Duerig, D. Stöckel, Minim. Invasive Ther. Allied Technol. 13 (2004) 218-221.
[20] J.I. Kim, S. Miyazaki, Acta Mater. 53 (2005) 4545-4554.
[21] Y. Zhou, J. Zhang, G. Fan, X. Ding, J. Sun, X. Ren, K. Otsuka, Acta Mater. 53 (2005) 5365-5377.
[22] C.P. Frick, A.M. Ortega, J. Tyber, A.E.M. Maksound, H.J. Maier, Y. Liu, K. Gall, Mater. Sci. Eng. A 405 (2005) 34-49.
[23] M. Paryab, J. Environ. Friendly Mater. 1 (2019) 23.
[24] K.S. Kim, K.K. Jee, W.C. Kim, W.Y. Jang, S.H. Han, Mater. Sci. Eng. A 481-482 (2008) 658-661.
[25] Z.X. Khoo, J. An, C.K. Chua, Y.F. Shen, C.N. Kuo, Y. Liu, Materials 12 (2019) 77.
[26] J.J. Marattukalam, V.K. Balla, M. Das, S. Bontha, S.K. Kalpathy, J. Alloy. Compd. 744 (2018) 337-346.
[27] J. Mentz, M. Bram, H.P. Buchkremer, D. Stöver, Mater. Sci. Eng. A 481-482 (2008) 630-634.
[28] K.W.K. Yeung, K.M.C. Cheung, W.W. Lu, C.Y. Chung, Mater. Sci. Eng. A 383 (2004) 213-218.
[29] A. Chmielewska, B. Wysocki, P. Kwaśniak, M.J. Kruszewski, B. Michalski, A. Zielińska,

B. Adamczyk-Cieślak, A. Krawczyńska, J. Buhagiar, W. Święszkowski, Materials 15 (2022) 3304.
[30] H.Z. Lu, L.H. Liu, C. Yang, X. Luo, C.H. Song, Z. Wang, J. Wang, Y.D. Su, Y.F. Ding, L.C. Zhang, Y.Y. Li, J. Mater. Sci. Technol. 101 (2022) 205-216.
[31] D. Ye, S.F. Li, R.D.K. Misra, R. Zheng, Y.F. Yang, Addit. Manuf. 47 (2021) 102344.
[32] S. Saedi, N. Shayesteh Moghaddam, A. Amerinatanzi, M. Elahinia, H.E. Karaca, Acta Mater. 144 (2018) 552-560.
[33] Z. Yu, Z. Xu, Y. Guo, R. Xin, R. Liu, C. Jiang, L. Li, Z. Zhang, L. Ren, J. Mater. Res. Technol. 13 (2021) 241-250.
[34] A.B. Spierings, M. Schneider, R. Eggenberger, Rapid Prototyp. J. 17 (2011) 380-386.
[35] M. Losertová, M. Štencek, D. Matýsek, O. Štefek, J. Drápala, IOP Conf. Ser. Mater. Sci. Eng. 266 (2017) 012008.
[36] S. Jiang, Y. Zhang, Y. Zhao, S. Liu, L. Hu, C. Zhao, Trans. Nonferrous Met. Soc. China 25 (2015) 4063-4071.
[37] J. Khalil-Allafi, A. Dlouhy, G. Eggeler, Acta Mater. 50 (2002) 4255-4274.
[38] Y. Feng, Z. Gao, Z. Hu, Materials 15 (2022) 3298.
[39] P. Bayati, K. Safaei, M. Nematollahi, A. Jahadakbar, A. Yadollahi, M. Mahtabi, M. Elahinia, Int. J. Adv. Manuf. Technol. 112 (2021) 347-360.
[40] K. Sugiyama, Y. Takéuchi, Z. Für Krist. - Cryst. Mater. 194 (1991) 305-314.
[41] R. Restori, D. Schwarzenbach, J.R. Schneider, Acta Crystallogr. B 43 (1987) 251-257.
[42] T.P. Feist, P.K. Davies, J. Solid State Chem. 101 (1992) 275-295.
[43] J.F. Banfield, D.R. Veblen, D.J. Smith, Am. Mineral. 76 (1991) 343-353.
[44] R. Marchand, L. Brohan, M. Tournoux, Mater. Res. Bull. 15 (1980) 1129-1133.
[45] H. Zhang, B. Wu, S. Wang, Mater. Des. 236 (2023) 112520.
[46] R.J. Warzoha, N.T. Vu, B.F. Donovan, E. Cimpoiasu, D.J. Sharar, A.C. Leff, A.A. Wilson, A.N. Smith, Int. J. Heat Mass Transf. 154 (2020) 119760.
[47] W. Pantleon, Scr. Mater. 58 (2008) 994-997.
[48] R. Mackay, G.J. Miller, H.F. Franzen, J. Alloy. Compd. 204 (1994) 109–118.
[49] L. Bumke, N. Wolff, C. Chluba, T. Dankwort, L. Kienle, E. Quandt, Shape Mem. Superelast. 7 (2021) 526–540.
[50] C.-H. Chen, Y.-C. Wang, S.-K. Wu, N.-H. Lu, J. Alloy. Compd. 810 (2019) 151904.
[51] J.X. Zhang, M. Sato, A. Ishida, Acta Mater. 51 (2003) 3121-3130.
[52] J. Bhagyaraj, K.V. Ramaiah, C.N. Saikrishna, S.K. Bhaumik, Gouthama, J. Alloy. Compd. 581 (2013) 344-351.
[53] N.N. Greenwood, A. Earnshaw, Chemistry of the Elements, Amsterdam: Elsevier, 2012.
[54] D. Holec, M. Friák, A. Dlouhý, J. Neugebauer, Phys. Rev. B 84 (2011) 224119.
[55] S. Liu, Y. Lin, G. Wang, X. Wang, Mater. Charact. 172 (2021) 110832.
[56] J. Michutta, Ch. Somsen, A. Yawny, A. Dlouhy, G. Eggeler, Acta Mater. 54 (2006) 3525-3542.
[57] A. Ahadi, E. Rezaei, J. Mater. Eng. Perform. 21 (2012) 1806-1812.
[58] G. Tadayyon, M. Mazinani, Y. Guo, S.M. Zebarjad, S.A.M. Tofail, M.J.P. Biggs, Mater. Charact. 112 (2016) 11-19.
[59] I. Ur Rehman, T.-H. Nam, Sci. Adv. Mater. 12 (2020) 1403-1408.
[60] J. Mentz, J. Frenzel, M.F.-X. Wagner, K. Neuking, G. Eggeler, H.P. Buchkremer, D. Stöver, Mater. Sci. Eng. A 491 (2008) 270-278.
[61] R. Yoshida, Y. Suzuki, S. Yoshikawa, J. Solid State Chem. 178 (2005) 2179-2185.
[62] A. Chmielewska, B. Wysocki, J. Buhagiar, B. Michalski, B. Adamczyk-Cieślak, M. Gloc, W. Święszkowski, Mater. Today Commun. 30 (2022) 103007.
[63] B. Feng, C. Wang, Q. Zhang, Y. Ren, L. Cui, Q. Yang, S. Hao, Mater. Sci. Eng. A 840 (2022) 142965.

[64] S. Sabbagh, M.A. Behnajady, Photochem. Photobiol. 95 (2019) 733-739.
[65] Z. Wang, Y. Wang, W. Zhang, Z. Wang, Y. Ma, X. Zhou, J. Phys. Chem. C 123 (2019) 1779-1789.
[66] P. Wang, J. Li, C.Z. Lin, L. Yang, C. Xiao, Trans. Nonferrous Met. Soc. China 26 (2016) 2546-2554.
[67] S.P. Gupta, K. Mukherjee, A.A. Johnson, Mater. Sci. Eng. 11 (1973) 283-297.
[68] H.F. López, A. Salinas-Rodríguez, J.L. Rodríguez-Galicia, Scr. Mater. 34 (1996) 659-664.
[69] T. Fukuda, T. Kakeshita, H. Houjoh, S. Shiraishi, T. Saburi, Mater. Sci. Eng. A 273-275 (1999) 166-169.
[70] W.-S. Ko, B. Grabowski, J. Neugebauer, Phys. Rev. B 92 (2015) 134107.
[71] L. Xun, L. Ying, L. Chang, W. Lu, L. Ruoshan, Mater. Today Commun. 36 (2023) 106526.
[72] X. Shao, X. Guo, Y. Han, Z. Lin, J. Qin, W. Lu, D. Zhang, J. Mater. Res. 29 (2014) 2707-2716.
[73] Y.H. Lv, J. Li, Y.F. Tao, L.F. Hu, Appl. Surf. Sci. 402 (2017) 478-494.
[74] R. Song, J. Li, J.Z. Shao, L.L. Bai, J.L. Chen, C.C. Qu, Appl. Surf. Sci. 355 (2015) 298-309.
[75] A. Undisz, F. Schrempel, W. Wesch, M. Rettenmayr, J. Biomed. Mater. Res. A 100A (2012) 1743-1750.
[76] P. Ninpetch, P. Kowitwarangkul, S. Mahathanabodee, R. Tongsri, P. Ratanadecho, IOP Conf. Ser. Mater. Sci. Eng. 526 (2019) 012030.
[77] I. Stachiv, E. Alarcon, M. Lamac, Metals 11 (2021) 415.
[78] Y. Liu, Y. Liu, J. Van Humbeeck, Acta Mater. 47 (1998) 199-209.
[79] S. Sanjabi, Z.H. Barber, Surf. Coat. Technol. 204 (2010) 1299-1304.